Multistable dissipative breathers and collective states in SQUID Lieb metamaterials

N. Lazarides[1,2] and G. P. Tsironis[1,2,3]
[1]*Department of Physics, University of Crete, P. O. Box 2208, 71003 Heraklion, Greece*
[2]*National University of Science and Technology "MISiS," Leninsky Prospekt 4, Moscow 119049, Russia*
[3]*School of Engineering and Applied Sciences, Harvard University, Cambridge, Massachusetts 02138, USA*

(Received 27 September 2017; revised manuscript received 9 May 2018; published 12 July 2018)

A SQUID (Superconducting QUantum Interference Device) metamaterial on a Lieb lattice with nearest-neighbor coupling supports simultaneously stable dissipative breather families which are generated through a delicate balance of input power and intrinsic losses. Breather multistability is possible due to the peculiar snaking flux amplitude-frequency curve of single dissipative-driven SQUIDs, which for relatively high sinusoidal flux field amplitudes exhibits several stable and unstable solutions in a narrow frequency band around resonance. These breathers are very weakly interacting with each other, while multistability regimes with a different number of simultaneously stable breathers persist for substantial intervals of frequency, flux field amplitude, and coupling coefficients. Moreover, the emergence of chimera states as well as temporally chaotic states exhibiting spatial homogeneity within each sublattice of the Lieb lattice is demonstrated. The latter of the states emerge through an explosive hysteretic transition resembling explosive synchronization that has been reported before for various networks of oscillators.

DOI: 10.1103/PhysRevE.98.012207

I. INTRODUCTION

Superconducting metamaterials, a particular class of artificial media which rely on the sensitivity of the superconducting state to external stimuli such as temperature and magnetic fields, reached by their constituting elements at low temperatures, have recently been the focus of considerable research efforts [1–3]. The superconducting analog of conventional (metallic) metamaterials, which can become nonlinear with the insertions of appropriate electronic components [4,5], are the SQUID (Superconducting QUantum Interference Device) metamaterials. The latter are inherently nonlinear due to the Josephson effect [6], since each SQUID, in its simplest version, consists of a superconducting ring interrupted by a Josephson junction (JJ). The concept of SQUID metamaterials was theoretically introduced more than a decade ago in both the quantum [7] and the classical [8] regimes. Recent experiments on SQUID metamaterials have revealed several extraordinary properties such as negative diamagnetic permeability [9,10], broad-band tunability [10,11], self-induced broad-band transparency [12], and dynamic multistability and switching [13], as well as coherent oscillations [14]. Moreover, nonlinear localization [15] and nonlinear band opening (nonlinear transmission) [16], as well as the emergence of dynamic states referred to as *chimera states* in current literature, have been demonstrated numerically in SQUID metamaterial models [17,18]. Those counterintuitive dynamic states have been discovered numerically in rings of identical phase oscillators [19] (see Ref. [20] for a review). Further metamaterial configurations that have been proposed, which incorporate JJs in their structure, include superconducting transmission lines interrupted by a single JJ which may act as a mirror that reflects photons in a broad range of frequencies [21], JJ transmission lines in which the junctions are regarded as "defects," to realize tunable Fabry-Perot filters [22], and thin metamaterial films containing JJs [23], as well as superconductive wave guides which are periodically loaded by JJs [24].

Experimental and theoretical investigations on SQUID metamaterials have been limited to quasi-one-dimensional (1D) lattices and two-dimensional (2D) tetragonal lattices. However, different arrangements of SQUIDs on the plane can be realized which may also give rise to band structures; for example, the arragnement of SQUIDs on a *line-centered tetragonal* (Lieb) lattice, which is described by three sites in a square unit cell [Fig. 1(a)], gives rise to a frequency spectrum featuring a Dirac cone intersected by a topological flat band. Such a *SQUID Lieb metamaterial* (SLiMM) supports compact flat-band localized states [25], very much alike to those observed in photonic Lieb lattices [26,27]. Here, the existence of simultaneously stable excitations of the form of dissipative discrete breathers (DBs) is demonstrated numerically for a SLiMM which is driven by a sinusoidal flux field and is subjected to dissipation. DBs are spatially localized and time-periodic excitations [28,29] whose existence has been proved rigorously for nonlinear Hamiltonian networks of weakly coupled oscillators [30,31]. They actually have been observed in several physical systems such as Josephson ladders [32] and Josephson arrays [33], micromechanical oscillator arrays [34], proteins [35], and antiferromagnets [36], among others. From the large volume of research work on DBs, only a very small fraction is devoted to dissipative breathers, e.g., in Josephson ladders [37,38], Frenkel-Kontorova lattices [38,39], 2D Josephson arrays [40], nonlinear metallic metamaterials [41], and 2D tetragonal SQUID metamaterials [15]. These excitations emerge through a delicate balance of input power and intrinsic losses. Dissipative beathers in Josephson arrays and ladders are reviewed in Ref. [42]; for a more general review, see Ref. [43]. Note that dissipative breathers may

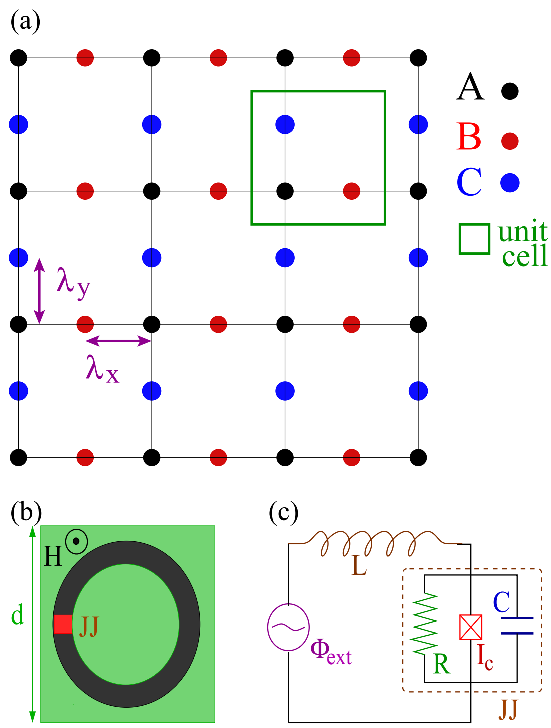

FIG. 1. (a) Schematic of a Lieb lattice; each unit cell (green square) has a corner SQUID (black) and two edge SQUIDs (red and blue). The nearest-neighbor coupling coefficients are indicated as λ_x and λ_y. (b) Schematic of a single SQUID. (c) Equivalent electrical circuit for a dissipative-driven SQUID.

exhibit richer dynamics than their Hamiltonian counterparts including quasiperiodic [38] and chaotic [37,38] behavior. Moreover, simple 1D and 2D tetragonal lattices are considered in most works, except, e.g., those on moving DBs in a 2D hexagonal lattice [44], on DBs in cuprate-like lattices [45], and on long-lived DBs in free-standing graphene (honeycomb lattice) [46].

In the following, the dynamic equations for the fluxes through the loops of the SQUIDs of a SLiMM are quoted. Then a typical bifurcation curve of the flux amplitude as a function of the driving frequency for a single SQUID is presented, which features a snaking form around resonance. Subsequently, its use for the construction of *trivial* dissipative DB configurations is explained. In this context, a *trivial breather* is an exact DB solution at the uncoupled (anticontinuous) limit of the SLiMM. The existence of simultaneously stable dissipative DBs (hereafter multistable DBs) at a frequency close to that of the single-SQUID resonance is demonstrated. Bifurcation curves for the multistable DB amplitudes with varying the external flux field amplitude, the coupling coefficients, and the frequency of the driving flux field are traced. For better understanding of those bifurcation diagrams, standard measures for energy localization and synchronization of coupled oscillators are calculated. Moreover, the existence of chimera states for appropriately chosen initial conditions is also demonstrated. Eventually, the wealth of dynamic behaviors that can be encountered in a SLiMM due to its lattice structure is indicated by the emergence of temporally chaotic states exhibiting a particular form of spatial coherence.

The knowledge of the dynamic behavior of SLiMMs in experimentally relevant parameter ranges could be very useful in designing practical devices. For example, dissipative DBs may act similarly to defects in JJ transmission lines [22,24], by filtering an incoming flux wave. The existence of multistable DB families and the possibility to switch between them allows for quantitative variation of the filtering properties. Furthermore, DB localized modes allow for engineering the band gaps and dispersion relation for flux wave propagation [21]. As it is known from SQUID metamaterials on tetragonal lattices, DBs alter locally the magnetic response of the metamaterial from paramagnetic to diamagnetic or vice versa [15], Since the DB modes presented below are rather compact, DB distributions in SLiMMs could be in principle employed to store information in magnetic form.

The chimera states demonstrated in Sec. V may find useful applications in understanding spatiotemporal patterns found in diverse physical systems and broaden our understanding of transitions from synchrony to "turbulence" and vice versa. Those counterintuitive states, whose number could be very large, coexist with synchronized low flux amplitude states in wide parameter intervals. This type of multistability can be utilized in various ways. Interestingly, different SLiMM states exhibit different values of effective magnetic permeability. The transition from a synchronized to a temporally chaotic state exhibits hysteresis, which can be utilized in fast switching applications.

II. FLUX DYNAMICS EQUATIONS

Consider the Lieb lattice of Fig. 1(a), in which each site is occupied by a SQUID [Fig. 1(b)] modeled by the equivalent circuit shown in Fig. 1(c); all the SQUIDs are identical, with each of them featuring a self-inductance L, a capacitance C, a resistance R, and a critical current of the Josephson junction I_c. The SQUIDs are magnetically coupled to their nearest neighbors along the horizontal (vertical) direction through their mutual inductance M_x (M_y). Assuming that the current in each SQUID is given by the resistively and capacitively shunted junction (RCSJ) model [47], the dynamic equations for the fluxes through the loops of the SQUIDs are [25]

$$LC\frac{d^2\Phi^A_{n,m}}{dt^2} + \frac{L}{R}\frac{d\Phi^A_{n,m}}{dt} + LI_c \sin\left(2\pi\frac{\Phi^A_{n,m}}{\Phi_0}\right) + \Phi^A_{n,m}$$
$$= \lambda_x(\Phi^B_{n,m} + \Phi^B_{n-1,m}) + \lambda_y(\Phi^C_{n,m} + \Phi^C_{n,m-1}) + [1 - 2(\lambda_x + \lambda_y)]\Phi_e, \quad (1)$$

$$LC\frac{d^2\Phi^B_{n,m}}{dt^2} + \frac{L}{R}\frac{d\Phi^B_{n,m}}{dt} + LI_c \sin\left(2\pi\frac{\Phi^B_{n,m}}{\Phi_0}\right) + \Phi^B_{n,m}$$
$$= \lambda_x(\Phi^A_{n,m} + \Phi^A_{n+1,m}) + (1 - 2\lambda_x)\Phi_e, \quad (2)$$

$$LC\frac{d^2\Phi^C_{n,m}}{dt^2} + \frac{L}{R}\frac{d\Phi^C_{n,m}}{dt} + LI_c \sin\left(2\pi\frac{\Phi^C_{n,m}}{\Phi_0}\right) + \Phi^C_{n,m}$$
$$= \lambda_y(\Phi^A_{n,m} + \Phi^A_{n,m+1}) + (1 - 2\lambda_y)\Phi_e, \quad (3)$$

where $\Phi^k_{n,m}$ is the flux through the loop of the SQUID of kind k in the (n,m)th unit cell [$k = A, B, C$; the notation follows that of Fig. 1(a)], $I^k_{n,m}$ is the current in the SQUID of kind k in the (n,m)th unit cell, Φ_0 is the flux quantum, $\lambda_x = M_x/L$ ($\lambda_y = M_y/L$) is the coupling coefficient along the horizontal (vertical) direction, t is the temporal variable, and $\Phi_e = \Phi_{ac}\cos(\omega t)$ is the external flux due to a sinusoidal magnetic field applied perpendicularly to the plane of the SLiMM. The subscript n (m) runs from 1 to N_x (1 to N_y), so that $N = N_x N_y$ is the number of unit cells of the SLiMM (the number of SQUIDs is $3N$).

Using the relations $\tau = \omega_{LC} t$, $\phi^k_{n,m} = \Phi^k_{n,m}/\Phi_0$, and $\phi_{ac} = \Phi_{ac}/\Phi_0$, where $\omega_{LC} = 1/\sqrt{LC}$ is the inductive-capacitive (LC) SQUID frequency, Eqs. (1)–(3) can be normalized as

$$\mathcal{L}\phi^A_{n,m} = \lambda_x\left(\phi^B_{n,m} + \phi^B_{n-1,m}\right) + \lambda_y\left(\phi^C_{n,m} + \phi^C_{n,m-1}\right) + [1 - 2(\lambda_x + \lambda_y)]\phi_e(\tau), \tag{4}$$

$$\mathcal{L}\phi^B_{n,m} = \lambda_x\left(\phi^A_{n,m} + \phi^A_{n+1,m}\right) + (1 - 2\lambda_x)\phi_e(\tau), \tag{5}$$

$$\mathcal{L}\phi^C_{n,m} = \lambda_y\left(\phi^A_{n,m} + \phi^A_{n,m+1}\right) + (1 - 2\lambda_y)\phi_e(\tau), \tag{6}$$

where

$$\beta = \frac{L\,I_c}{\Phi_0} = \frac{\beta_L}{2\pi} \quad \text{and} \quad \gamma = \omega_{LC}\frac{L}{R} \tag{7}$$

is the dimensionless SQUID parameter and loss coefficient, respectively, $\phi_e(\tau) = \phi_{ac}\cos(\Omega\tau)$ is the external flux of frequency $\Omega = \omega/\omega_{LC}$ and amplitude ϕ_{ac}, and $\mathcal{L}$ is an operator such that

$$\mathcal{L}\phi^k_{n,m} = +\ddot{\phi}^k_{n,m} + \gamma\dot{\phi}^k_{n,m} + \phi^k_{n,m} + \beta\sin\left(2\pi\phi^k_{n,m}\right). \tag{8}$$

The overdots on $\phi^k_{n,m}$ denote differentiation with respect to τ.

The SQUID parameter and the loss coefficient used in the simulations have been chosen to be the same as those provided in the Supplemental Material of Ref. [12] for a 11×11 SQUID metamaterial, i.e., $\beta_L = 0.86$ and $\gamma = 0.01$. These values result from Eq. (7) with $L = 60\,pH$, $C = 0.42\,pF$, $I_c = 4.7\,\mu A$, and subgap resistance $R = 500$ Ohms. The value of the coupling between neighboring SQUIDs has been chosen to be $\lambda_x = \lambda_y = -0.02$, as has been estimated for a 27×27 SQUID metamaterial in the experiments of Ref. [11]. These experiments were performed with a specially designed setup which allows for the application of almost uniform ac driving and/or dc bias fluxes [11,12] as well as dc flux gradients [14] to the SQUID metamaterials which are placed into a waveguide. In the simulation results presented in the next sections, the described effects can be identified within the experimentally accessible range of ϕ_{ac} which spans the interval 0.001–0.1 [12]. Furthermore, the SLiMM is chosen to have 16×16 unit cells, so that its size is comparable with that of the 27×27 SQUID metamaterial investigated in Refs. [11,14].

In the next three sections, several dynamic states of the SLiMM are presented; a common feature between them is their *spatial nonuniformity*. For the detection and visualization of spatially nonuniform SQUID metamaterial states, a method relying on the cryogenic laser scanning microscope (LSM) has been recently developed [48–50]. The versatility of that method was demonstrated with an array of SQUIDs by visualizing its microwave response (rf currents) on a scale ranging from the whole array down to its individual elements. The LSM experiments show that this technique is a powerful tool for spatially resolved characterization of planar metamaterials and may be useful for their optimization. Importantly, direct visualization of spatially localized excitations in a 27×27 SQUID metamaterial has been recently reported [50].

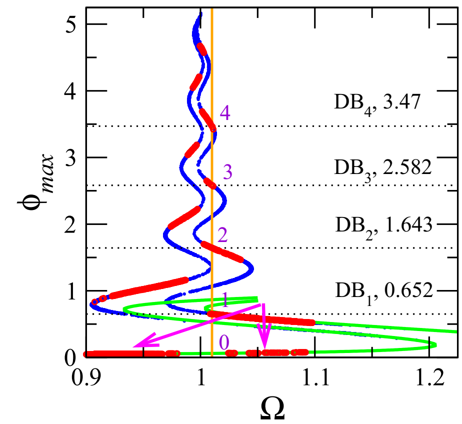

FIG. 2. The snaking flux amplitude $\phi_{\max}$-driving frequency Ω curve for a single SQUID with $\beta_L = 0.86$ and $\phi_{ac} = 0.05$ (blue curves). The green curves are calculated from Eq. (10). The vertical orange line is at frequency $\Omega = 1.01$ ($T = 2\pi/\Omega = 6.22$). The red symbols superposed on some branches of the $\phi_{\max}$-Ω curve are the amplitudes of *stable* dissipative discrete breather families (except the ones indicated by the arrows; see text).

III. SINGLE SQUID RESONANCE AND MULTISTABLE DISSIPATIVE BREATHERS

In a single SQUID driven with a relatively high-amplitude field ϕ_{ac}, strong nonlinearities shift the resonance frequency from $\Omega = \Omega_{SQ}$ to $\Omega \sim 1$, i.e., to the LC frequency ω_{LC}. Moreover, the curve for the oscillation amplitude of the flux through the loop of the SQUID $\phi_{\max}$ as a function of the driving frequency Ω (SQUID resonance curve) acquires a snaking form as that shown in Fig. 2 (blue) [18]. That curve is calculated from the normalized single SQUID equation

$$\ddot{\phi} + \gamma\dot{\phi} + \beta\sin(2\pi\phi) + \phi = \phi_{ac}\cos(\Omega\tau), \tag{9}$$

for the flux ϕ through the loop of the SQUID. The curve “snakes” back and forth within a narrow frequency region via successive saddle-node bifurcations (occurring at those points for which $d\Omega/d\phi_{\max} = 0$). The many branches of the resonance curve have been traced numerically using Newton's method; the stable branches are those which are partially covered by the red circles. An approximation to the resonance curve for $\phi_{\max} \ll 1$ is given by [18]

$$\Omega^2 = \Omega_{SQ}^2 \pm \frac{\phi_{ac}}{\phi_{\max}} - \beta_L\phi_{\max}^2 \times \left\{a_1 - \phi_{\max}^2\left[a_2 - \phi_{\max}^2\left(a_3 - a_4\phi_{\max}^2\right)\right]\right\}, \tag{10}$$

where $a_1 = \pi^2/2$, $a_2 = \pi^4/12$, $a_3 = \pi^6/144$, and $a_4 = \pi^8/2880$, which implicitly provides $\phi_{\max}(\Omega)$. The approximate curves (10) are shown in Fig. 2 in green; they show excellent agreement with the numerical snaking resonance curve for $\phi_{\max} \lesssim 0.6$. The vertical orange segment at $\Omega = 1.01$ intersects the resonance curve at several $\phi_{\max}$ points; five of those, numbered in Fig. 2 with consecutive integers from 0 to 4, correspond to stable solutions of the single

SQUID equation. These five solutions, which can be denoted as $(\phi_i,\dot{\phi}_i)$ with $i = 0,1,2,3,4$, are used for the construction of four trivial dissipative DB configurations. Note that the flux amplitude $\phi_{\max}$ of these five solutions increases with increasing i. For constructing a (single-site) trivial dissipative DB, two simultaneously stable solutions are first identified, say, $(\phi_0,\dot{\phi}_0)$ (0) and $(\phi_1,\dot{\phi}_1)$ (1), with low and high flux amplitude $\phi_{\max}$, respectively. Then one of the SQUIDs, say, that at $(n,m) = (n_e = N_x/2, m_e = N_y/2)$ (hereafter referred to as the central DB site, which also determines the location of the DB), is set to the high flux amplitude solution 1, while all the other SQUIDs of the SLiMM (the background) are set to the low flux amplitude solution 0. In order to numerically obtain a dissipative DB, that trivial DB configuration is used as the initial condition for the time integration of Eqs. (4)–(6); then a stable dissipative DB (denoted as DB_1) is formed after time integration for a few thousand time units. Three more trivial dissipative DBs can be constructed similarly, e.g., by setting the central DB site to the solution 2, 3, or 4, and the background to the solution 0. Then, by integrating Eqs. (4)–(6) using as initial conditions these trivial DB configurations, three more stable dissipative DBs are obtained numerically (denoted as DB_2, DB_3, and DB_4, respectively). These four dissipative DBs are simultaneously stable and oscillate with the driving frequency $\Omega = 1.01$.

The Hamiltonian (total energy) for the SLiMM described by Eqs. (4)–(6) for $\gamma = 0$ is given by

$$H = \sum_{n,m} H_{n,m}, \tag{11}$$

where the Hamiltonian (energy) density, $H_{n,m}$, is

$$\begin{aligned} H_{n,m} = {} & \frac{\pi}{\beta} \sum_k \left[\left(q_{n,m}^k\right)^2 + \left(\phi_{n,m}^k - \phi_e\right)^2 \right] \\ & - \sum_k \cos\left(2\pi \phi_{n,m}^k\right) \\ & - \frac{\pi}{\beta} \{ \lambda_x [(\phi_{n,m}^A - \phi_e)(\phi_{n-1,m}^B - \phi_e) \\ & + 2(\phi_{n,m}^A - \phi_e)(\phi_{n,m}^B - \phi_e) \\ & + (\phi_{n,m}^B - \phi_e)(\phi_{n+1,m}^A - \phi_e)] \\ & + \lambda_y [(\phi_{n,m}^A - \phi_e)(\phi_{n,m-1}^C - \phi_e) \\ & + 2(\phi_{n,m}^A - \phi_e)(\phi_{n,m}^C - \phi_e) \\ & + (\phi_{n,m}^C - \phi_e)(\phi_{n,m+1}^A - \phi_e)] \}, \end{aligned} \tag{12}$$

where $q_{n,m}^k = \frac{d\phi_{n,m}^k}{d\tau}$ is the normalized instantaneous voltage across the JJ of the SQUID in the (n,m)th unit cell of kind k. Both H and $H_{n,m}$ are normalized to the Josephson energy, E_J. Two more quantities are also defined: the *energetic participation ratio* [51,52]

$$epr = \left[\sum_{n,m} \left(\frac{H_{n,m}}{H} \right)^2 \right]^{-1}, \tag{13}$$

which is a measure of localization (it roughly measures the number of the excited unit cells), and the complex *synchronization parameter* originally introduced by Kuramoto (Kuramoto order parameter)

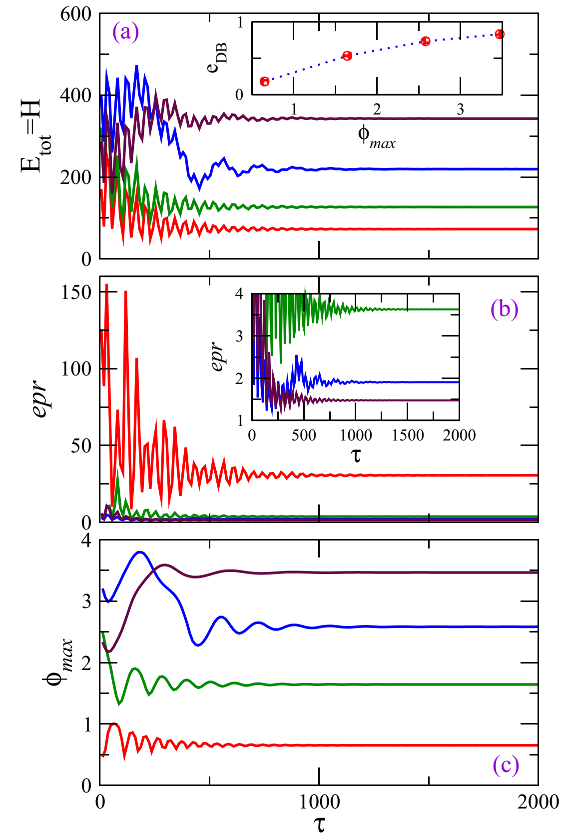

FIG. 3. (a) The total energy $E_{\text{tot}} = H$ of the SQUID Lieb metamaterial as a function of τ for $N_x = N_y = 16$, $\beta_L = 0.86$, $\lambda_x = \lambda_y = -0.02$, $\gamma = 0.01$, $\Omega = 1.01$, $\phi_{ac} = 0.05$, and four initial conditions-trivial breather configurations. Inset: The ratio $e_{\text{DB}} \equiv H_{n=n_e,m=m_e}/H$ as a function of the steady-state dissipative breather amplitude $\phi_{\max}$ for the four multistable dissipative breathers. The blue-dotted curve is a guide to the eye. (b) The energetic participation ratio *epr* as a function of τ for the four initial conditions-trivial breather configurations. Inset: The *epr* as a function of τ for the trivial breather configurations leading to the three more localized dissipative breathers. (c) The amplitude of the four multistable dissipative breathers $\phi_{\max}$ as a function of τ. The asymptotic values of $\phi_{\max}$ have been used in the inset in (a).

$$\Psi = \frac{1}{3N} \sum_{n,m,k} e^{2\pi i \phi_{n,m}^k}, \tag{14}$$

which is a spatially global measure of synchronization for coupled oscillators; its magnitude $r(\tau) = |\Psi(\tau)|$ ranges from zero (completely desynchronized solution) to unity (completely synchronized solution).

Equations (4)–(6) implemented with periodic boundary conditions are initialized with the four trivial breather configurations and then integrated in time with a standard Runge-Kutta fourth order scheme. The temporal evolution of the total energy of the SLiMM $H(\tau)$, the energetic participation ratio $epr(\tau)$, and the dissipative DB amplitude $\phi_{\max}(\tau)$ are shown for all cases in Fig. 3. After some oscillations during the initial stages of evolution, all curves flatten, indicating that a steady state has been reached (after ∼1500 time units of integration). As can be

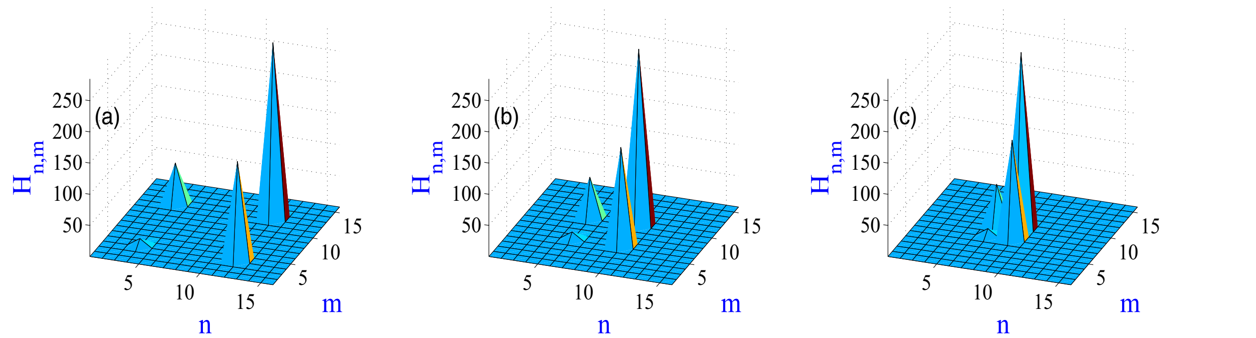

FIG. 4. The energy density $H_{n,m}$ of the SQUID Lieb metamaterial on the n-m plane, in which four dissipative breathers exist simultaneously, for $N_x = N_y = 16$, $\beta_L = 0.86$, $\gamma = 0.01$, $\lambda_x = \lambda_y = -0.02$, $\Omega = 1.01$, $\phi_{ac} = 0.05$, and different separations. The central breather sites for DB_1, DB_2, DB_3, and DB_4, are located on a square with vertices, respectively, at (a) $(n_e,m_e) = (4,4),(4,12),(12,4),(12,12)$; (b) $(n_e,m_e) = (6,6),(6,10),(10,6),(10,10)$; (c) $(n_e,m_e) = (7,7),(7,9),(9,7),(9,9)$.

observed, the SLiMM has higher energy for higher amplitude DBs, $\phi_{\max}$ [Fig. 3(a)]. The steady-state values of $\phi_{\max}$ for the four multistable DBs can be seen in Fig. 3(c); these values have been also used in the inset of Fig. 3(a). In that inset, the ratio of the energy of the unit cell to which the central DB site belongs over the total energy of the SLiMM, i.e., $e_{\rm DB} = H_{n_e,m_e}/H$, is shown for the four DBs. This ratio increases considerably with increasing DB amplitude. This is certainly compatible with Fig. 3(b) (see also the inset), in which *epr* is plotted as a function of τ, where apparently higher amplitude DBs provide more localized structures than lower amplitude ones.

It is convenient to present the energy density $H_{n,m}$ profiles of the four dissipative DBs in one plot, as shown in Fig. 4. These profiles are obtained after $2000T \simeq 12\,500$ time units of time integration ($T = 2\pi/\Omega$), using an appropriate initial condition which is a combination of the four trivial DB configurations. The difference between the three subfigures is in the distances between the central DB sites. Remarkably, the steady-state total energy of the SLiMM, $H = E_{\rm tot}$, is the same in all the three cases and equal to $H = 580.6$, indicating that the interaction between these DBs is almost negligible, even if they are located very closely [as in Fig. 4(c)].

IV. BIFURCATIONS OF MULTISTABLE DISSIPATIVE BREATHERS

In this section, the parameter intervals in which these four DBs are stable are determined; for this purpose, the steady-state DB amplitudes $\phi_{\max}$ are calculated as a function of either the driving flux field amplitude ϕ_{ac}, the magnitude of the coupling coefficients $\lambda_x = \lambda_y$ (isotropic coupling), or the driving frequency Ω. First, $\phi_{\max}$, the energetic participation ratio *epr*, and the magnitude of the synchronization parameter averaged over the steady-state integration time $\tau_{\rm int} = 2000T$ time units (transients have been discarded) are calculated as a function of ϕ_{ac} (Fig. 5). In Fig. 5(a) it can be seen that higher amplitude DBs remain stable for narrower intervals of ϕ_{ac}. Interestingly, higher amplitude DBs may turn into lower amplitude ones even several times until they completely disappear. As an example, we note that DB_4 (blue curve), which is stable approximately for ϕ_{ac} between 0.04 and 0.085, transforms to a DB_2 for $\phi_{ac} < 0.04$, and then to an even lower amplitude DB for $\phi_{ac} < 0.015$. The presence of the latter DB is rather unexpected, since it cannot be identified with one of the four DB families under consideration. All the DBs disappear for $\phi_{ac} \lesssim 0.005$, since the nonlinearity is not strong enough to localize energy in the SLiMM. For ϕ_{ac} exceeding a critical

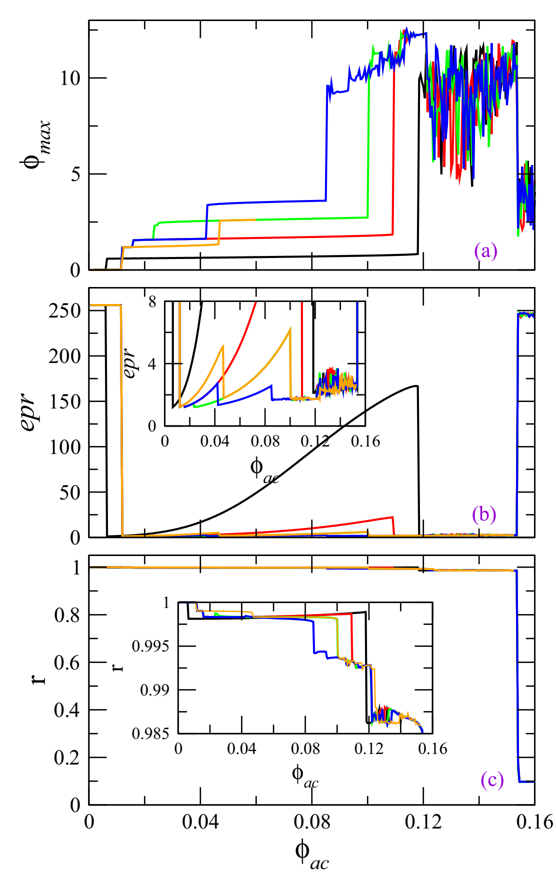

FIG. 5. (a) The four dissipative breather amplitudes $\phi_{\max}$ as a function of the driving field amplitude ϕ_{ac}, for $N_x = N_y = 16$, $\beta_L = 0.86$, $\gamma = 0.01$, $\Omega = 1.01$, and $\lambda_x = \lambda_y = -0.02$. (b) The corresponding energetic participation ratios *epr* as a function of ϕ_{ac}. Inset: Enlargement for low *epr* values. (c) The corresponding magnitudes of the synchronization parameter averaged over the steady-state integration time $\langle r \rangle_{\rm int}$ as a function of ϕ_{ac}. Inset: Enlargement for values of $\langle r \rangle_{\rm int} \lesssim 1$.

value, which is higher for lower amplitude DBs (e.g., 0.085 for DB_4 and 0.118 for DB_1), all the four DBs turn into irregular multibreather states.

In Figs. 5(b) and 5(c) the corresponding *epr* and $\langle r \rangle_{\text{int}}$ are presented as a function of ϕ_{ac}. In Fig. 5(b), it can be seen that when all the DBs disappear for low ϕ_{ac}, the SLiMM reaches a homogeneous state which is advocated by the large, close to the maximum possible value of $epr \simeq N = 256$. In that case, $\langle r \rangle_{\text{int}}$ is exactly unity [Fig. 5(c)] since the homogeneous state is synchronized. For high values of ϕ_{ac} ($\phi_{ac} > 0.118$), where $\phi_{\max}$ for all the four DBs varies irregularly with varying ϕ_{ac}, the value of *epr* can be used to distinguish between two different regimes: the first one from $\phi_{ac} \simeq 0.118$ to 0.154, in which the low, fluctuating value of *epr* suggests the existence of (possibly chaotic) multibreathers [see also the inset of Fig. 5(b)], and the second from $\phi_{ac} \simeq 0.154$ to 0.16, in which the high value of *epr* ($\simeq$256) suggests the existence of a desynchronized state in which all the units cells are excited. For intermediate values of ϕ_{ac}, *epr* generally increases with increasing ϕ_{ac}; in particular, for DB_1 it increases to rather high values because of the relative enhancement of the oscillation amplitude of the background unit cells with respect to the central DB unit cell. However, this is not observed for the high-amplitude DBs, for which the increase is either moderate (as in DB_2) or very small (as in DB_3 and DB_4). It is also apparent that whenever a DB is transformed to another, a small jump in *epr* occurs (inset). Figure 5(c) provides useful information on the synchronization of the various SLiMM states. For example, for $\phi_{ac} \simeq 0.154$ to 0.16, $\langle r \rangle_{\text{int}}$ falls off to very low values indicating desynchronization as mentioned above. For the values of ϕ_{ac} which provide stable single-site DBs that belong to one of the four families (as well as the fifth one which has appeared), the measure $\langle r \rangle_{\text{int}}$ is always very close to unity (inset); that occurs because all the "background" SQUIDs are oscillating in phase with the same amplitude, and only one SQUID (at the central DB site) is oscillating with higher amplitude while its phase is the opposite with respect to those of the others. For low ϕ_{ac}, the SLiMM reaches a homogeneous state (the DBs have disappeared) and then $\langle r \rangle_{\text{int}}$ is exactly unity.

The corresponding diagram of the DB flux amplitudes $\phi_{\max}$ as a function of the coupling coefficients $\lambda_x = \lambda_y = \lambda$ (isotropic coupling) is shown in Fig. 6. Remarkably, the four DBs maintain their amplitudes almost constant for a substantial interval of λ [Fig. 6(a)], i.e., from $\lambda = 0$ to -0.026, which includes the estimated physically acceptable values for that system [11,14]. The corresponding values of the *epr* remain low, except for the lowest amplitude breather (DB_1), for which $epr \simeq 30$. Note that DB_1 disappears for $\lambda > -0.003$, but it exists all the way down to $\lambda = -0.05$. For large magnitudes of λ, the amplitudes of the three high-amplitude breathers (DB_2, DB_3, and DB_4) vary irregularly with varying λ; however, as can be observed in Fig. 6(b), their *epr* remains relatively low, possibly indicating the spontaneous formation of multibreathers.

The bifurcation diagram of the DB flux amplitudes $\phi_{\max}$ as a function of the driving frequency Ω is particularly interesting. This diagram has been superposed on the single SQUID resonance curve shown in Fig. 2 as red circles. Notice that DB flux amplitudes (i.e., the flux amplitudes of the central DB site) which are shown as red circles, are very close to the corresponding flux amplitudes of single-SQUID stable solutions (which

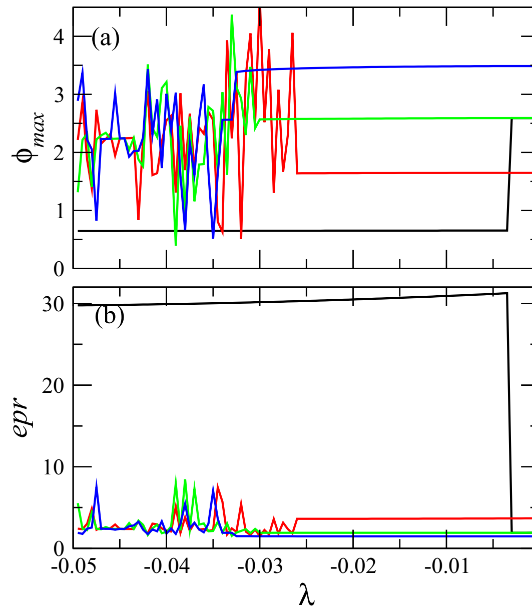

FIG. 6. (a) The flux amplitudes $\phi_{\max}$ of the four dissipative breather families as a function of the coupling coefficients $\lambda_x = \lambda_y = \lambda$, for $N_x = N_y = 16$, $\beta_L = 0.86$, $\gamma = 0.01$, $\Omega = 1.01$, and $\phi_{ac} = 0.05$. (b) The corresponding energetic participation ratios *epr* as a function of λ.

are covered by the red circles). All red-circled branches (except the lowest ones pointed by the arrows) correspond to stable DB families. The branches indicated by the arrows correspond to almost homogeneous solutions which are not DBs. Note that a different number of multistable dissipative DBs exists for different driving frequencies, depending on the broadness of the red-circled branches; for example, for $\Omega = 1.01$ there are four multistable DBs, while for $\Omega = 1.03$ there are two, and for $\Omega = 1.07$ there is only one stable DB.

V. NOVEL DYNAMIC SLIMM STATES

So far, we focused on the formation of single-site, dissipative DBs in a SLiMM, which can be generated through trivial DB configurations, and they are simultaneously stable. Beyond such solutions, other interesting numerical solutions have been obtained; they correspond to counterintuitive dynamic states such as the so-called chimera states and a new type of states that exhibit spatial homogeneity as well as chaotic evolution. Typical examples of such states are demonstrated here. First, a chimera state solution is illustrated which is generated from the initial condition

$$\phi_{n,m}^k(\tau = 0) = \begin{cases} 0.5, & \text{if } N_x/4 + 1 < n \leqslant 3N_x/4 \\ & \text{and } N_y/4 + 1 < m \leqslant 3N_y/4; \\ 0, & \text{otherwise} \end{cases} \quad (15)$$

and

$$\dot{\phi}_{n,m}^k(\tau = 0) = 0, \quad \text{for any } n, m. \quad (16)$$

With Eqs. (15) and (16) as initial conditions, Eqs. (4)–(6) for the SLiMM are integrated in time with periodic boundary conditions. The magnitude of the synchronization parameter averaged over each driving period $T = 2\pi/\Omega$, $\langle r \rangle_T(\tau)$, is

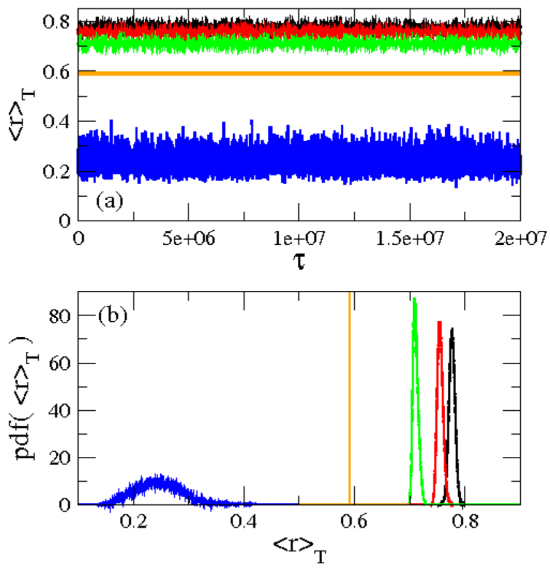

FIG. 7. (a) The synchronization parameter averaged over the driving period T, $\langle r\rangle_T$, as a function of τ for $N_x = N_y = 16$, $\beta = 0.86$, $\gamma = 0.01$, $\lambda_x = \lambda_y = -0.02$, $\phi_{ac} = 0.1$, and $\Omega = 1.01$ (black); $\Omega = 1.02$ (red); $\Omega = 1.03$ (green); $\Omega = 1.04$ (blue); $\Omega = 1.05$ (orange). (b) The corresponding probability distribution functions $pdf(\langle r\rangle_T)$ normalized to unity area. The actual peak of the orange curve, which is practically a δ function is at $pdf(\langle r\rangle_T) = 8000$.

monitored in time, and the results are shown in Fig. 7(a) for five different driving frequencies Ω close to unity. It can be seen that $\langle r\rangle_T(\tau)$ is in all cases considerably less than unity, indicating significant desynchronization. The fluctuations, however, of $\langle r\rangle_T(\tau)$ do not all have the same size. Specifically, for $\Omega = 1.01$, 1.015, and 1.02 (black, red, and green curves, respectively), the fluctuations have roughly the same size. For $\Omega = 1.025$ (blue curve), the size of fluctuations is significantly larger, while for $\Omega = 1.03$ (orange curve) the fluctuations are practically zero. This can be seen more clearly in Fig. 7(b), in which the distributions $pdf(\langle r\rangle_T)$ of the values of $\langle r\rangle_T(\tau)$ are shown; the full-width half-maximum (FWHM) of the $pdf(\langle r\rangle_T)$s quantifies the level of metastability of chimera states [53,54]. A partially desynchronized dynamic state with $\langle r\rangle_T < 1$ but practically zero fluctuations is not a chimera state but is another clustered state in which different groups of SQUIDs oscillate with different amplitudes and phases with respect to the driving field; however, the SQUID oscillators that belong to the same group are synchronized with each other. Thus, as can be inferred from Fig. 7 as well as by the inspection of the flux profiles at the end of integration time (not shown), the curves for $\Omega = 1.01$, 1.015, 1.02, and 1.025 (black, red, green, and blue curves, respectively) are indeed due to chimera states. The energy density profiles at the end of the integration time for $\Omega = 1.01$, 1.03, and 1.05 are shown in Fig. 8. The first two are typical for chimera states, while the last one is typical for the other clustered state described earlier. Note that the SQUIDs within the square into which the fluxes were initialized to a nonzero value oscillate with high amplitude, and they are not synchronized. The rest of the SQUIDs, i.e., those outside that square, oscillate in phase and with the same (low) amplitude. Thus, from the initial condition (15) and (16), different chimera states are obtained for different driving frequencies. These states differ in their asymptotic value of $\langle r\rangle_T$ as well as the FWHM of their $pdf(\langle r\rangle_T)$s which determines their metastability level. In Fig. 8(c), on the other hand, one may distinguish easily groups of SQUIDs with the same amplitude. The SQUIDs that belong to such a group are synchronized together while the groups are not synchronized with each other. In this state, all the SQUIDs are oscillating with high amplitude (note the energy scales).

A family of solutions emerges through an order-to-chaos phase transition that occurs at a critical value of a control parameter which varies within a certain interval. Below, the ac flux amplitude ϕ_{ac} has been chosen as that parameter. Equations (4)–(6) with periodic boundary conditions are integrated in time for ϕ_{ac} increasing from zero to higher values; the initial condition is homogeneous, i.e., $\phi_{n,m}^k(\tau = 0) = \dot{\phi}_{n,m}^k(\tau = 0) = 0$ for any n, m, and k. The ac flux field amplitude ϕ_{ac} increases in small steps, and for each step the solution for the previous step is taken as the initial condition. For relatively low ϕ_{ac}, the amplitudes of the oscillating fluxes through the loops of the SQUIDs have low values, and they are very close to each other, i.e., $\phi_{\max}^A \simeq \phi_{\max}^B = \phi_{\max}^C$ as shown in Fig. 9(a) (all the SQUIDs of kind k are oscillating with amplitude $\phi_{\max}^k$, $k = A,B,C$). Actually, the difference between $\phi_{\max}^A$ and $\phi_{\max}^{B,C}$

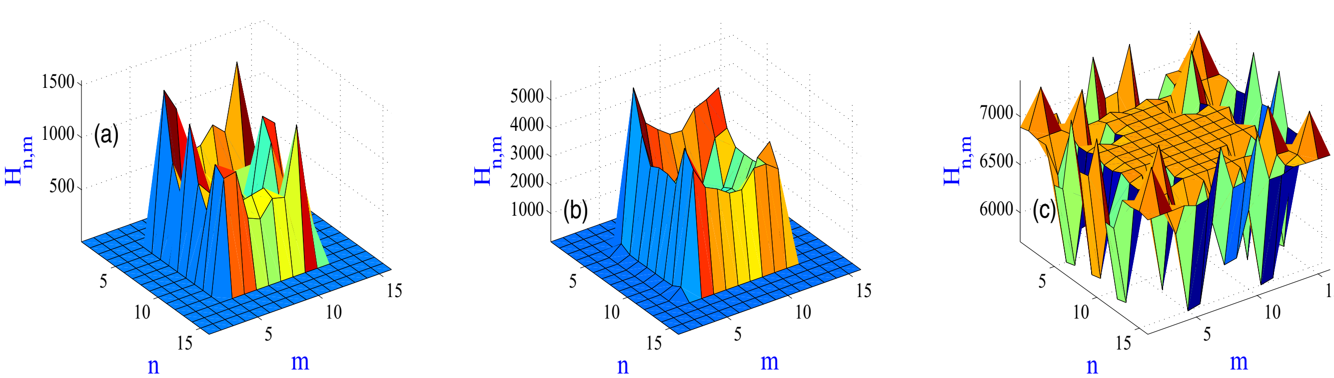

FIG. 8. The energy density $H_{n,m}$ of the SQUID Lieb metamaterial (energy per unit cell) on the n-m plane, after integrating the dynamic equations for $10^7 T$ time units, for $N_x = N_y = 16$, $\beta_L = 0.86$, $\gamma = 0.01$, $\lambda_x = \lambda_y = -0.02$, $\phi_{ac} = 0.1$, and (a) $\Omega = 1.01$; (b) $\Omega = 1.03$; (c) $\Omega = 1.05$. The value of the synchronization parameter averaged over the steady-state integration time is $\langle r\rangle_{\rm int} \sim 0.77$, ~ 0.71, and ~ 0.59, respectively.

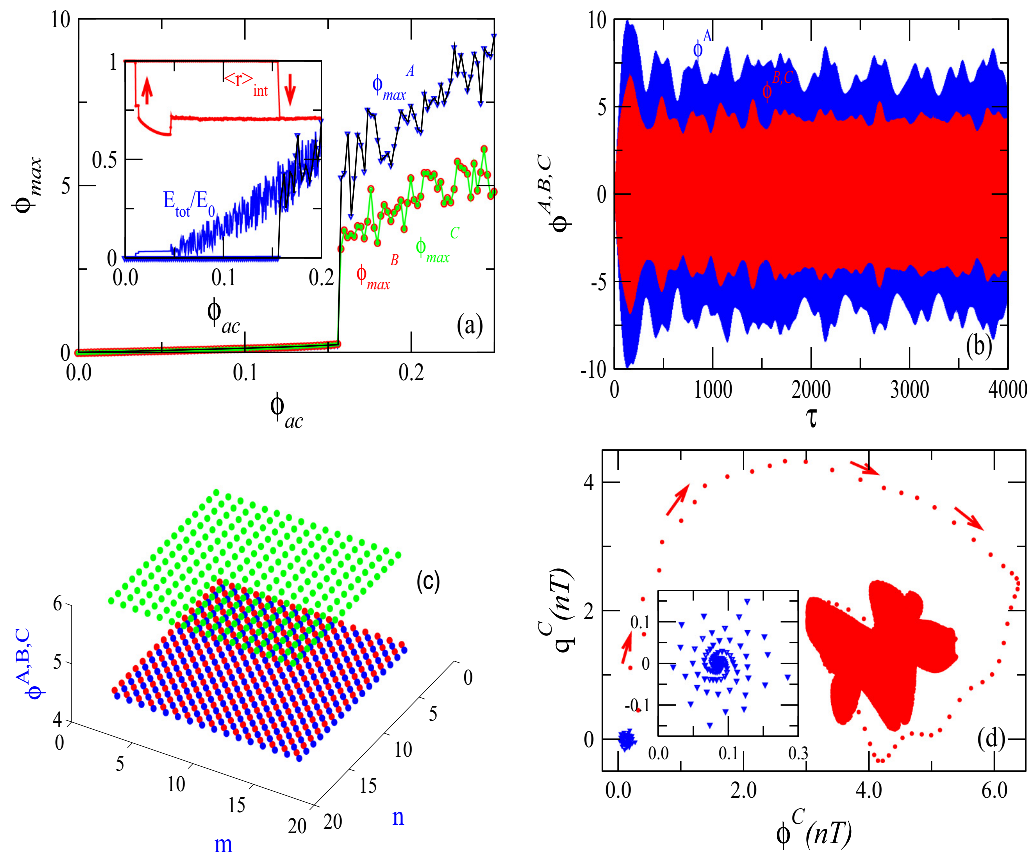

FIG. 9. (a) The flux oscillation amplitudes $\phi_{\max}^A$, $\phi_{\max}^B$, and $\phi_{\max}^C$ of the SQUIDs of kind A (blue), B (red), and C (green), respectively, of the (n_e,m_e)th unit cell as a function of the driving flux field amplitude ϕ_{ac} for $N_x = N_y = 16$, $\beta_L = 0.86$, $\gamma = 0.01$, $\Omega = 1.01$, and $\lambda_x = \lambda_y = -0.02$. Inset: The magnitude of the synchronization parameter averaged over the steady-state integration time $\langle r\rangle_{\rm int}$ (red) and the total energy of the SQUID Lieb metamaterial divided by $E_0 = 10^6$, $E_{\rm tot}/E_0$ (blue), as a function of ϕ_{ac}. Note the large hysteresis region in those curves. (b) Time dependence of ϕ^A (blue), ϕ^B (red), and ϕ^C (green), for $\phi_{ac} = 0.2$ and the other parameters as in (a). (c) The fluxes ϕ^A (green), ϕ^B (red), and ϕ^C (blue), on the n-m plane for $\phi_{ac} = 0.2$ and the other parameters as in (a). (d) Stroboscopic plots of $\phi^C(nT) - q^C(nT)$, with $q^C \equiv \dot{\phi}^C$, for $\phi_{ac} = 0.1$ (blue) and $\phi_{ac} = 0.2$ (red). An enlargement of the period-1 attractor is shown in the inset. The red arrows are along the transient leading to the chaotic attractor.

is less than 1% in this regime. Moreover, the fluxes in all kinds of SQUIDs are oscillating periodically in phase, and thus the degree of synchronization $\langle r\rangle_{\rm int}$ of these states is almost unity [see the upper branch of the red curve in the inset of Fig. 9(a)]. That state is referred to as an *almost homogeneous state* in space. In the inset of Fig. 9(a), the total energy of the SLiMM $E_{\rm tot} = H$ divided by $E_0 = 10^6$ is plotted as a function of ϕ_{ac}; that energy increases smoothly with increasing ϕ_{ac} [lower branch of the blue curve in the inset of Fig. 9(a)]. At a critical value of ϕ_{ac}, $\phi_{ac}^c \simeq 0.155$, the situation changes drastically, as an abrupt increase of all the amplitudes $\phi_{\max}^k$ occurs while their values become considerably different ($\phi_{\max}^A$ attains considerably larger values than $\phi_{\max}^B = \phi_{\max}^C$). Moreover, for $\phi_{ac} > \phi_{ac}^c$, the values of $\phi_{\max}^k$s vary irregularly with increasing ϕ_{ac}, although their average values as well as the difference between $\phi_{\max}^A$ and $\phi_{\max}^{B,C}$ increase [Fig. 9(a)]. Also, at the phase transition point ϕ_{ac}^c, the parameter $\langle r\rangle_{\rm int}$ abruptly jumps to a value which indicates significant desynchronization, $\langle r\rangle_{\rm int} \sim 0.7$; that value remains almost unchanged with further increasing ϕ_{ac} (inset). The variation of the total energy of the SLiMM $E_{\rm tot}$ is similar to that of the variation of the $\phi_{\max}^k$, i.e., it jumps abruptly to higher values at $\phi_{ac} = \phi_{ac}^c$ (inset). Recall that the above remarks hold for ϕ_{ac} increasing from zero to higher values. The corresponding curves for $\langle r\rangle_{\rm int}$ and $E_{\rm tot}$ for ϕ_{ac} decreasing from 0.3 to zero are also shown in the inset of Fig. 9(a) (lower branch of the red curve and upper branch of the blue curve, respectively). The explosive character of the transition resembles that of the synchronization in scale-free Kuramoto networks [55], in networked chaotic oscillators [56], and in complex neural networks [57], among others.

Consider again the case in which ϕ_{ac} increases from zero to higher values. In that case, the steady states of the SLiMM are almost synchronized (almost spatially homogeneous) and temporally periodic for $\phi_{ac} < \phi_{ac}^c$. Note, however, that those states are exactly homogeneous at the unit cell level, i.e., that $\bar{\phi}_{n,m} = \sum_k \phi_{n,m}^k = c$ for any n and m, with c being a constant. For $\phi_{ac} > \phi_{ac}^c$ the SLiMM states acquire chaotic time dependence, while they retain partial homogeneity and thus synchronization; that is, all the SQUIDs of kind k are synchronized while they execute chaotic oscillations. Remarkably, at the unit cell level, even this state is spatially homogeneous. In Fig. 9(b) the time dependence of the fluxes ϕ^A, ϕ^B, and ϕ^C (identical for all the SQUID of kind A, B, and C, respectively, of the SLiMM) are plotted for $\phi_{ac} = 0.2$ during a few thousands time units. Apparently, the flux oscillations are irregular, indicating chaotic behavior which has been checked to persists for very long times (note that $\phi^B = \phi^C$ due to the isotropic coupling). A flux profile for that state is shown in Fig. 9(c), in which the spatial homogeneity within each sublattice of the SLiMM is apparent. Thus, large-scale synchronization between oscillators in a chaotic state occurs in this case. In Fig. 9(d) two stroboscopic plots in the reduced ϕ^C - $\dot{\phi}^C$ ($\dot{\phi}^C = q^C$) phase space are shown together for the C SQUID at the (n_e, m_e)th unit cell. The stroboscopic period is equal to that of the driving flux, i.e., $T = 2\pi/\Omega = 6.22$ ($\Omega \simeq 1.01$). In the first one (blue down-triangles, inset), the SLiMM is in an almost synchronized temporally periodic state ($\phi_{ac} = 0.1$); in the the second one (red circles), the SLiMM is in a partially synchronized (synchronization of the SQUIDs within each sublattice) temporally chaotic state ($\phi_{ac} = 0.2$). Apparently, the trajectory in the reduced phase space tends to a point in the former case, while it tends to a large area attractor in the latter. In Fig. 9(d) the transients leading the trajectories to the one or the other attractor are also shown.

VI. CONCLUSIONS

The extremelly rich dynamic behavior of SLiMMs is explored numerically, and different types of solutions are demonstrated. The most relevant findings of this work are the following.

(1) The existence of several regions in parameter space in which simultaneously stable dissipative DBs exist in a SLiMM driven by a sinusoidal flux field. For that purpose, Eqs. (4)–(6) for the fluxes threading the loops of the SQUIDs are integrated in time with periodic boundary conditions. The initial conditions are trivial single-site DB configurations, which have been constructed using the simultaneously stable solutions of the single-SQUID oscillator. The bifucation diagrams for the calculated DB amplitudes as a function of ϕ_{ac}, λ, and Ω have been presented. Remarkably, the interactions between coexisting DBs are very weak.

The bifurcation diagram of the dissipative DB amplitudes as a function of Ω, shown as the branches formed by the red circles in Fig. 2, resembles the snaking bifurcation curves for spatially localized states in the Swift-Hohenberg equation [58,59]. Similar snaking bifurcation curves have been also reported for 1D [60,61] and 2D bistable lattices [62]. Furthermore, snaking bifurcation diagrams for chimera states have been obtained in the 1D extended Bogdanov-Takens lattice [63].

(2) The existence of chimera states, which can be generated in a SLiMM by appropriate choice of initial conditions. Such counter-intuitive dynamic states have been demonstrated in 1D SQUID metamaterials, with both local and nonlocal coupling between the SQUIDs [17,18]. The key ingredient for their existence is the multistability of individual SQUIDs around resonance which gives rise to the *attractor crowding* effect [64,65] in SQUID metamaterials. Similar chimera states are also expected to appear in SQUID metamaterials on tetragonal lattices.

(3) The transition of the sinusoidally driven SLiMM from a low-amplitude, spatially homogeneous state to a high-amplitude, temporally chaotic state as the ac flux amplitude ϕ_{ac} exceeds a critical value ϕ_{ac}^c. The temporally chaotic state exhibits partial homogeneity within each sublattice of the Lieb lattice; however, it is spatially homogeneous at the unit cell level. These states, which exhibit large-scale chaotic synchronization [66,67], are peculiar to the lattice geometry of the SLiMM (Lieb lattice). The order-to-chaos transition with hysteresis obtained here is similar to that demonstrated numerically and observed in laser-cooled trapped ions [68].

The solutions described in (1) and (2) depend crucially on the choice of the initial conditions, i.e., the initial state of the SLiMM. The SLiMM could be in principle excited to such an initial state by, e.g., incorporating into the experimental arrangement a small circular coil through which microwave flux pulses may excite a number of SQUIDs into a high-amplitude state [13]. The power and the duration of those pulses would then determine roughly the number of the most strongly excited SQUIDs. Subsequent evolution of such initial states by sweeping up and down the ac flux amplitude may give rise to either highly localized (DB) of chimera states.

ACKNOWLEDGMENTS

This work is partially supported by the Ministry of Education and Science of the Russian Federation in the framework of the Increase Competitiveness Program of NUST "MISiS" (No. K2-2017-006), and by the European Union under project NHQWAVE (MSCA-RISE 691209). N.L. gratefully acknowledges the Laboratory for Superconducting Metamaterials, NUST "MISiS," for its warm hospitality during visits.

[1] S. M. Anlage, The physics and applications of superconducting metamaterials, J. Opt. **13**, 024001 (2011).
[2] P. Jung, A. V. Ustinov, and S. M. Anlage, Progress in superconducting metamaterials, Supercond. Sci. Technol. **27**, 073001 (2014).
[3] N. Lazarides and G. P. Tsironis, Superconducting metamaterials, Phys. Rep. (2018), doi: 10.1016/j.physrep.2018.06.005.
[4] M. Lapine, M. Gorkunov, and K. H. Ringhofer, Nonlinearity of a metamaterial arising from diode insertions into resonant conductive element, Phys. Rev. E **67**, 065601 (2003).
[5] M. Lapine, I. V. Shadrivov, and Y. S. Kivshar, *Colloquium*: Nonlinear metamaterials, Rev. Mod. Phys. **86**, 1093 (2014).
[6] B. Josephson, Possible new effects in superconductive tunnelling, Phys. Lett. A **1**, 251 (1962).
[7] C. Du, H. Chen, and S. Li, Quantum left-handed metamaterial from superconducting quantum-interference devices, Phys. Rev. B **74**, 113105 (2006).
[8] N. Lazarides and G. P. Tsironis, rf superconducting quantum interference device metamaterials, Appl. Phys. Lett. **90**, 163501 (2007).
[9] P. Jung, S. Butz, S. V. Shitov, and A. V. Ustinov, Low-loss tunable metamaterials using superconducting circuits with Josephson junctions, Appl. Phys. Lett. **102**, 062601 (2013).

[10] S. Butz, P. Jung, L. V. Filippenko, V. P. Koshelets, and A. V. Ustinov, A one-dimensional tunable magnetic metamaterial, Opt. Express **21**, 22540 (2013).

[11] M. Trepanier, Daimeng Zhang, O. Mukhanov, and S. M. Anlage, Realization and Modeling of Rf Superconducting Quantum Interference Device Metamaterials, Phys. Rev. X **3**, 041029 (2013).

[12] D. Zhang, M. Trepanier, O. Mukhanov, and S. M. Anlage, Broadband Transparency of Macroscopic Quantum Superconducting Metamaterials, Phys. Rev. X **5**, 041045 (2015).

[13] P. Jung, S. Butz, M. Marthaler, M. V. Fistul, J. Leppäkangas, V. P. Koshelets, and A. V. Ustinov, Multistability and switching in a superconducting metamaterial, Nat. Commun. **5**, 3730 (2014).

[14] M. Trepanier, Daimeng Zhang, O. Mukhanov, V. P. Koshelets, P. Jung, S. Butz, E. Ott, T. M. Antonsen, A. V. Ustinov, and S. M. Anlage, Coherent oscillations of driven rf SQUID metamaterials, Phys. Rev. E **95**, 050201(R) (2017).

[15] N. Lazarides, G. P. Tsironis, and M. Eleftheriou, Dissipative discrete breathers in rf SQUID metamaterials, Nonlinear Phenom. Complex Syst. **11**, 250 (2008).

[16] G. P. Tsironis, N. Lazarides, and I. Margaris, Wide-band tuneability, nonlinear transmission, and dynamic multistability in SQUID metamaterials, Appl. Phys. A **117**, 579 (2014).

[17] N. Lazarides, G. Neofotistos, and G. P. Tsironis, Chimeras in SQUID metamaterials, Phys. Rev. B **91**, 054303 (2015).

[18] J. Hizanidis, N. Lazarides, and G. P. Tsironis, Robust chimera states in SQUID metamaterials with local interactions, Phys. Rev. E **94**, 032219 (2016).

[19] Y. Kuramoto and D. Battogtokh, Coexistence of coherence and incoherence in nonlocally coupled phase oscillators, Nonlinear Phenom. Complex Syst. **5**, 380 (2002).

[20] M. J. Panaggio and D. M. Abrams, Chimera states: Coexistence of coherence and incoherence in network of coupled oscillators, Nonlinearity **28**, R67 (2015).

[21] D. Zueco, C. Fernández-Juez, J. Yago, U. Naether, B. Peropadre, J. J. García-Ripoll, and J. J. Mazo, From Josephson junction metamaterials to tunable pseudo-cavities, Supercond. Sci. Technol. **26**, 074006 (2013).

[22] V. Pierro and G. Filatrella, Fabry-Perot filters with tunable Josephson junction defects, Physica C **517**, 37 (2015).

[23] A. I. Maimistov and I. R. Gabitov, Nonlinear response of a thin metamaterial film containing Josephson junctions, Opt. Commun. **283**, 1633 (2010).

[24] H. R. Mohebbi and A. H. Majedi, Shock wave generation and cut off condition in nonlinear series connected discrete Josephson transmission line, IEEE Trans. Appl. Supercond. **19**, 891 (2009).

[25] N. Lazarides and G. P. Tsironis, SQUID metamaterials on a Lieb lattice: From flat-band to nonlinear localization, Phys. Rev. B **96**, 054305 (2017).

[26] R. A. Vicencio, C. Cantillano, L. Morales-Inostroza, B. Real, C. Mejía-Cortés, S. Weimann, A. Szameit, and M. I. Molina, Observation of Localized States in Lieb Photonic Lattices, Phys. Rev. Lett. **114**, 245503 (2015).

[27] S. Mukherjee, A. Spracklen, D. Choudhury, N. Goldman, P. Öhberg, E. Andersson, and R. R. Thomson, Observation of a Localized Flat-Band State in a Photonic Lieb Lattice, Phys. Rev. Lett. **114**, 245504 (2015).

[28] S. Flach and A. V. Gorbach, Discrete breathers—Advances in theory and applications, Phys. Rep. **467**, 1 (2008).

[29] S. Flach, Discrete breathers in a nutshell, Nonlinear Theory and Its Applications, IEICE **3**, 1 (2012).

[30] R. S. MacKay and S. Aubry, Proof of existence of breathers for time—Reversible or Hamiltonian networks of weakly coupled oscillators, Nonlinearity **7**, 1623 (1994).

[31] S. Aubry, Breathers in nonlinear lattices: Existence, linear stability and quantization, Physica D **103**, 201 (1997).

[32] P. Binder, D. Abraimov, A. V. Ustinov, S. Flach, and Y. Zolotaryuk, Observation of Breathers in Josephson Ladders, Phys. Rev. Lett. **84**, 745 (2000).

[33] E. Trías, J. J. Mazo, and T. P. Orlando, Discrete Breathers in Nonlinear Lattices: Experimental Detection in a Josephson Array, Phys. Rev. Lett. **84**, 741 (2000).

[34] M. Sato, B. E. Hubbard, A. J. Sievers, B. Ilic, D. A. Czaplewski, and H. G. Graighead, Observation of Locked Intrinsic Localized Vibrational Modes in a Micromechanical Oscillator Array, Phys. Rev. Lett. **90**, 044102 (2003).

[35] J. Edler, R. Pfister, V. Pouthier, C. Falvo, and P. Hamm, Direct Observation of Self-Trapped Vibrational States in α-helices, Phys. Rev. Lett. **93**, 106405 (2004).

[36] U. T. Schwarz, L. Q. English, and A. J. Sievers, Experimental Generation and Observation of Intrinsic Localized Spin Wave Modes in an Antiferromagnet, Phys. Rev. Lett. **83**, 223 (1999).

[37] P. J. Martínez, L. M. Floría, F. Falo, and J. J. Mazo, Intrinsically localized chaos in discrete nonlinear extended systems, Europhys. Lett. **45**, 444 (1999).

[38] P. J. Martínez, M. Meister, L. M. Floria, and F. Falo, Dissipative discrete breathers: Periodic, quasiperiodic, chaotic, and mobile, Chaos **13**, 610 (2003).

[39] J. L. Marín, F. Falo, P. J. Martínez, and L. M. Floría, Discrete breathers in dissipative lattices, Phys. Rev. E **63**, 066603 (2001).

[40] J. J. Mazo, Discrete Breathers in Two-Dimensional Josephson-Junction Arrays, Phys. Rev. Lett. **89**, 234101 (2002).

[41] N. Lazarides, M. Eleftheriou, and G. P. Tsironis, Discrete Breathers in Nonlinear Magnetic Metamaterials, Phys. Rev. Lett. **97**, 157406 (2006).

[42] J. J. Mazo and T. P. Orlando, Discrete breathers in Josephson arrays, Chaos **13**, 733 (2003).

[43] S. Flach and A. V. Gorbach, Discrete breathers with dissipation, Lect. Notes Phys. **751**, 289 (2008).

[44] J. L. Marín, J. C. Eilbeck, and F. M. Russell, Localized moving breathers in a 2D hexagonal lattice, Phys. Lett. A **248**, 225 (1998).

[45] J. L. Marín, F. M. Russell, and J. C. Eilbeck, Breathers in cuprate-like lattices, Phys. Lett. A **281**, 21 (2001).

[46] A. Fraile, E. N. Koukaras, K. Papagelis, N. Lazarides, and G. P. Tsironis, Long-lived discrete breathers in free-standing graphene, Chaos Solitons Fractals **87**, 262 (2016).

[47] K. K. Likharev, *Dynamics of Josephson Junctions and Circuits* (Gordon and Breach, Philadelphia, 1986).

[48] A. P. Zhuravel, A. V. Ustinov, and S. M. Anlage, Laser scanning microscopy of superconducting electromagnetic metamaterials, in *Proceedings of the 9th International Kharkiv Symposium on Physics and Engineering of Microwaves, Millimeter and Submillimeter Waves (MSMW)* (IEEE, Piscataway, 2016) .

[49] A. S. Averkin, A. P. Zhuravel, P. Jung, N. Maleeva, V. P. Koshelets, L. V. Filippenko, A. Karpov, and A. V. Ustinov, Imaging coherent response of superconducting metasurface, IEEE Trans. Appl. Supercond. **26**, 1 (2016).

[50] A. P. Zhuravel, A. V. Ustinov, M. Trepanier, Daimeng Zhang, and S. M. Anlage, Imaging microwave response of rf-SQUID metasurface in dc magnetic field, in *Proceedings of the 9th International Kharkiv Symposium on Physics and Engineering of Microwaves, Millimeter and Submillimeter Waves (MSMW)* (IEEE, Piscataway, 2016).

[51] F. A. B. F. de Moura, M. D. Coutinho-Filho, E. P. Raposo, and M. L. Lyra, Delocalization in harmonic chains with long-range correlated random masses, Phys. Rev. B **68**, 012202 (2003).

[52] T. V. Laptyeva, J. D. Bodyfelt, and S. Flach, Subdiffusion of nonlinear waves in two-dimensional disordered lattices, Europhys. Lett. **98**, 60002 (2012).

[53] N. Lazarides and G. P. Tsironis, Nonlinear localization in metamaterials, in *Nonlinear, Tunable and Active Metamaterials*, edited by I. Shadrivov, M. Lapine, and Yu. S. Kivshar (Springer, Cham, Switzerland, 2015), pp. 281–301.

[54] M. Shanahan, Metastable chimera states in community-structured oscillator networks, Chaos **20**, 013108 (2010).

[55] J. Gömez-Gardenes, S. Gömez, A. Arenas, and Y. Moreno, Explosive Synchronization Transitions in Scale-Free Networks, Phys. Rev. Lett. **106**, 128701 (2011).

[56] I. Leyva, R. Sevilla-Escoboza, J. M. Buldu, I. Sendina-Nadal, J. Gömez-Gardenes, A. Arenas, Y. Moreno, S. Gömez, R. Jaimes-Reategui, and S. Boccaletti, Explosive First-Order Transition to Synchrony in Networked Chaotic Oscillators, Phys. Rev. Lett. **108**, 168702 (2012).

[57] H. Chen, G. He, F. Huang, C. Shen, and Z. Hou, Explosive synchronization transitions in complex neural networks, Chaos **23**, 033124 (2013).

[58] E. Knobloch, Spatially localized structures in dissipative systems: Open problems, Nonlinearity **21**, T45 (2008).

[59] A. Bergeon, J. Burke, E. Knobloch, and I. Mercader, Eckhaus instability and homoclinic snaking, Phys. Rev. E **78**, 046201 (2008).

[60] C. Taylor and J. H. P. Dawes, Snaking and isolas of localised states in bistable discrete lattices, Phys. Lett. A **375**, 14 (2010).

[61] J. E. Prilepsky, A. V. Yulin, M. Johansson, and S. A. Derevyanko, Discrete solitons in coupled active lasing cavities, Opt. Lett. **37**, 4600 (2012).

[62] A. D. Dean, P. C. Matthews, S. M. Cox, and J. R. King, Orientation-dependent pinning and homoclinic snaking on a planar lattice, SIAM J. Appl. Dyn. Syst. **14**, 481 (2015).

[63] M. G. Clerc, S. Coulibaly, M. A. Ferré, M. A. García-Nustes, and R. G. Rojas, Chimera-type states induced by local coupling, Phys. Rev. E **93**, 052204 (2016).

[64] K. Wiesenfeld and P. Hadley, Attractor Crowding in Oscillator Arrays, Phys. Rev. Lett. **62**, 1335 (1989).

[65] K. Y. Tsang and K. Wiesenfeld, Attractor crowding in Josephson junction arrays, Appl. Phys. Lett. **56**, 495 (1990).

[66] L. M. Pecora and T. L. Carroll, Synchronization in Chaotic Systems, Phys. Rev. Lett. **64**, 821 (1990).

[67] J. F. Heagy, T. L. Carroll, and L. M. Pecora, Synchronous chaos in coupled oscillator systems, Phys. Rev. E **50**, 1874 (1994).

[68] J. Hoffnagle, R. G. DeVoe, L. Reyna, and R. G. Brewer, Order-Chaos Transition of Two Trapped Ions, Phys. Rev. Lett. **61**, 255 (1988).